



## Research article

# Label-free white blood cells classification using a deep feature fusion neural network

Jin Chen<sup>1</sup>, Liangzun Fu<sup>1</sup>, Maoyu Wei, Sikai Zheng, Jingwen Zheng, Zefei Lyu, Xiwei Huang\*, Lingling Sun

Ministry of Education Key Laboratory of RF Circuits and Systems, Hangzhou Dianzi University, Hangzhou, 310018, Zhejiang, China

## ARTICLE INFO

**Keywords:**

Label-free  
WBC classification  
Feature fusion  
Neural network  
Biomedical diagnosis

## ABSTRACT

White blood cell (WBC) classification is a valuable diagnostic approach for identifying diseases. However, conventional methods for WBC detection, such as flow cytometers, have limitations in terms of their high cost, large system size, and laborious staining procedures. As a result, deep learning-based label-free WBC image analysis methods are gaining popularity. Nevertheless, most existing deep learning WBC classification techniques fail to effectively utilize the subtle differences in the internal structures of WBCs observed under a microscope. To address this issue, we propose a neural network with feature fusion in this study, which enables the detection of label-free WBCs. Unlike conventional convolutional neural networks (CNNs), our approach combines low-level features extracted by shallow layers with high-level features extracted by deep layers, generating fused features for accurate bright-field WBC identification. Our method achieves an accuracy of 80.3 % on the testing set, demonstrating a potential solution for deep-learning-based biomedical diagnoses. Considering the proposed method simplifies the cell detection process and eliminates the need for complex operations like fluorescent staining, we anticipate that this automatic and label-free WBC classification network could facilitate more precise and effective analysis, and it could contribute to the future adoption of miniaturized flow cytometers for point-of-care (POC) diagnostics applications.

## 1. Introduction

Differential counts of white blood cells (WBCs) form a crucial factor for assessing the individual's health status [1–3]., WBCs can be categorized into three subtypes, namely granulocytes, lymphocytes, and monocytes, based on their unique characteristics such as nucleolus morphology [4]. These subtypes maintain a specific proportion in a healthy state. Changes in the morphology and percentage of various WBC subtypes are closely linked to disease diagnosis [5,6], such as leukemia and anemia. Therefore, accurate classification of WBCs is a prerequisite for precise treatment [7].

Typically, WBCs can be classified using two main approaches: manual and automatic. The traditional approach heavily relies on the expertise and experience of pathologists, making it a time-consuming and labor-intensive process. Importantly, although manual classification is the most direct approach, it is susceptible to inevitable errors. Consequently, the accuracy of this method heavily relies on the skills and knowledge of the pathologists. Automatic approaches for classifying WBCs may employ instruments such as flow

\* Corresponding author.

E-mail address: [huangxiwei@hdu.edu.cn](mailto:huangxiwei@hdu.edu.cn) (X. Huang).

<sup>1</sup> These authors contributed equally to this work.

cytometers [8]. These instruments utilize laser beams to stimulate WBCs labeled with fluorescent markers and use the resulting photoelectric signals for analysis. While flow cytometers yield high-throughput and high-accuracy results, they encounter challenges in terms of popularity due to their high cost and bulky nature. Consequently, flow cytometers are currently limited in their applicability for point-of-care (POC) WBC classification and find primary usage in established laboratory settings [9–12]. Importantly, staining procedures represent a crucial concern for the aforementioned methods as they can lead to cellular damage due to phototoxicity caused by fluorescent reagents, resulting in alterations in the morphology and physiological state of WBCs, such as the *ex vivo* activation of granulocytes.

In the past few years, the advent of deep learning has facilitated the development of automated systems for classifying WBCs [13]. Nonetheless, effectively harnessing the intricate information for accurate WBC identification continues to pose a significant challenge. In previous research work, deep learning for cell classification has mostly been conducted on stained cell images, as they contain more features, making them easier to be classified. For example, Dong et al. proposed a WBC recognition algorithm that fuses deep learning features with artificial features, achieving high accuracy in classifying stained WBC images [14]. Girdhar et al. achieved an accuracy of 98.55 % using custom-designed convolutional neural network (CNN) on a publicly available stained WBC dataset [15]. Jung et al. proposed a CNN model named W-Net to classify stained WBC images. It was first trained over a local dataset and then was used to classify the LISC dataset [16,17]. Wijesinghe et al. used k-means clustering for WBC nuclei segmentation from stained WBC images [18]. Thereafter, VGG-16 [19] classifier was used for putting WBC nuclei into their respective class. Gao et al. proposed a deep learning network similar to LeNet-5 for the successful classification of HEP-2 cells [20]. Similarly, Toratani et al. utilized VGG-16 [19] to differentiate between cancer cell lines and their corresponding radioresistant clones [21].

There are also some research work that focuses on label-free WBC classification. Li et al. achieved high accuracy in label-free WBC classification, but they utilized a complex holographic imaging system to obtain holographic cell images [22]. Nassar et al. also achieved an average F1 score of 97 % in label-free WBC classification and differentiated B and T lymphocytes with an average F1 score of 78 % [12]. However, they primarily relied on flow cytometry for the preceding steps and used machine learning for the final classification task. Ryu et al. proposed a rapid and accurate blood cell identification method exploiting deep learning and label-free refractive index tomography and achieved high accuracy in classifying bone marrow WBCs. The refractive index tomograms of the images are acquired via Mach-Zehnder interferometer-based tomographic microscope [23]. In this study, we strive to minimize the incorporation of additional steps to streamline complexity, leveraging the strengths of neural network to accomplish label-free WBC classification.

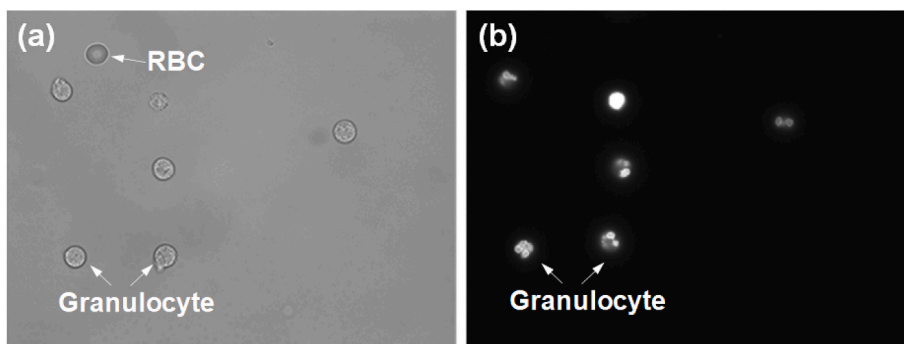
In order to leverage the subtle differences in the internal structures of WBCs captured through microscopy, this study proposes a neural network with feature fusion to enable label-free WBC detection. Unlike existing CNNs [19,24], this network fuses low-level features extracted by the shallow layers with high-level features extracted by deep layers into fused features for WBCs identification. This combination enhances the representation of WBCs by incorporating both detailed information from low-level features and semantic information from high-level features. In comparison to the previous immunofluorescence-based method [25], this work is promising as it eliminates the need for complex staining procedures and avoids the issue of photobleaching [26].

To evaluate the performance, we set the batch size to 128 images, then conducted 47 iterations to predict the subtype of the entire testing set, achieving an accuracy of 80.3 %. This achievement offers a promising solution for deep-learning-based biomedical diagnoses. By leveraging the method proposed in this paper, which simplifies cell detection and circumvents complex procedures like fluorescent staining, we anticipate the development of an automatic, label-free, and non-invasive WBC classification network based on microscope images. Such advancements could facilitate the widespread adoption of miniaturized flow cytometers for POC diagnostics applications, enabling more precise and effective analysis.

## 2. Material and methods

### 2.1. Label-free WBCs dataset generation

As there is no recognized label-free WBCs dataset specifically designed for classification tasks, we need to custom-build our dataset



**Fig. 1.** Example of (a) bright-field WBC image and corresponding (b) fluorescent image from the same field of view.

from scratch. The first step was to separate the WBCs from whole blood samples to reduce interference from red blood cells when imaging. The blood samples were obtained from Research Blood Components, LLC (Boston, MA, USA). The initial samples were sourced from healthy blood donors who underwent detailed health examinations before donation and had not used any prescription medications in the two weeks prior to donation. A multi-dimensional double spiral (MDDS) microfluidic cell separation device was utilized for WBC separation from blood, which can efficiently obtain high purity WBCs with minimum damages [27]. After the separation process, the WBCs were fluorescently stained and imaged using a microscope with a 100 × objective lens, alternating between bright-field and fluorescence modes in the same field of view (FOV). Note that the purpose of fluorescence staining is to obtain the true labels of bright-field cell images. In fluorescence imaging, granulocytes exhibit multiple distinct streaky bright spots due to their prominent nuclear lobulation structure. Monocytes and lymphocytes, on the other hand, display a round bright spot in fluorescence imaging as their nuclear structures appear similar. However, due to differences in nuclear size, lymphocytes appear similar in size under both bright-field and fluorescence imaging, while monocytes exhibit smaller bright spots in fluorescence imaging compared to bright-field imaging. Fig. 1 shows an example of bright-field WBC image and the corresponding fluorescent WBC image from the same FOV. The study was conducted according to the guidelines of the Declaration of Helsinki, and approved by the Ethics Committee of Westlake University (protocol code 20200608YY001) on June 06, 2020.

Following imaging, based on the grayscale differences between the foreground WBCs and the background, an adaptive threshold segmentation algorithm OTSU [28] was used to segment the WBCs from the background, ensuring that each image contained only a single WBC. With these, the original bright-field microscopic WBC images could be segmented to single-cell images with 200 × 200 pixel dimensions. We used the fluorescent images to manually label the subtypes of the bright-field images, ultimately dividing them into three categories: granulocyte, lymphocyte, and monocyte. To minimize the impact of fluorescent staining on cell viability as much as possible, we imaged the cells shortly after staining and manually selected well-shaped cells. This approach helps to exclude damaged cells or the cells in activation state, and reduce the influence of fluorescent staining process on the experimental results. The workflow for establishing the label-free WBC dataset is shown in Fig. 2(a–e).

As the proportions of different subtypes of WBCs in human blood are varied, the number of WBC images can often be unbalanced among different subtypes. To improve training accuracy and prevent overfitting problems during the training phase, we performed further balancing of the WBC dataset during the preprocessing stage. Initially, the original dataset was divided into two parts, with 80 % of the WBC images being used for training and validation, and the remaining 20 % for testing. Then, each independent dataset was enhanced to avoid any data leakage issue that could lead to overestimation of the test accuracy. Common data enhancement methods include rotation, flipping, scaling, color transformation, noise disturbance, etc. However, as the bright-field microscope images of WBCs are grayscale and rely on the morphological details of cells for classification, we only applied two enhancement methods of

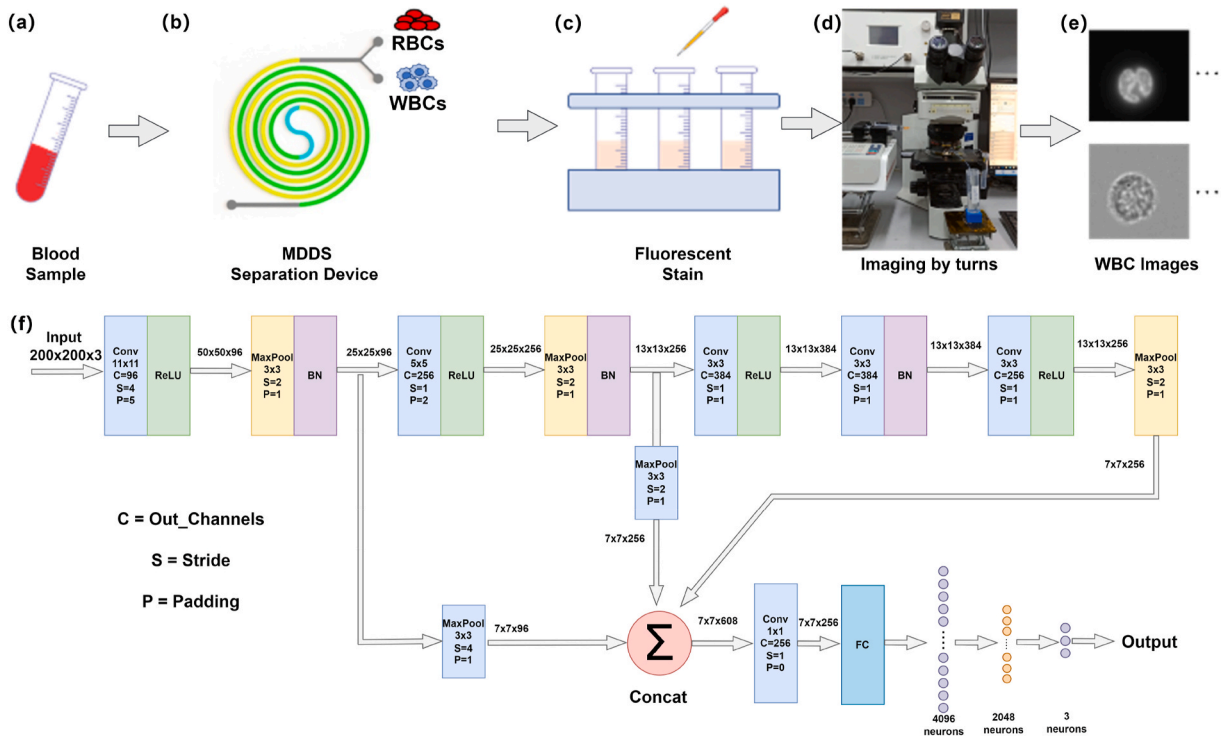


Fig. 2. (a) Whole blood samples. (b) MDDS separation device to separate blood samples into WBCs and RBCs. (c) fluorescently stain different subtypes of WBCs. (d) image WBCs with bright-field and fluorescence mode by turns. (e) segment WBCs from the background while manually mark the subtype of bright-field images. (f) Convolutional neural network structure diagram with feature fusion structure.

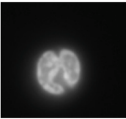
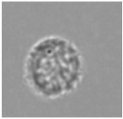
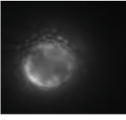
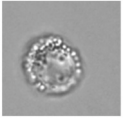

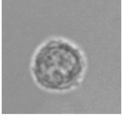
rotation and flipping to expand the dataset for all three types of WBCs. Moreover, we avoided using noise disturbance to prevent significant degradation of the images. We choose to use flipping and rotation as data augmentation methods based on their simplicity and effectiveness. Additionally, due to the minimal differences between unlabeled WBC images of various types, these methods do not lead to the loss of detail in cell images. This is because they solely perform geometric transformations on the images without altering their internal structure or features. In contrast, other augmentation techniques, such as blurring, distortion, or adding noise, may introduce more complexity and potentially degrade image quality or distort features. Therefore, we believe that flipping and rotation are simple yet effective methods that not only increase data samples but also preserve the integrity of image details, contributing to improved model performance and robustness. We left-right and up-down flipped all WBC images and rotated them by  $90^\circ$ ,  $180^\circ$ , and  $270^\circ$ , leading to a  $6 \times$  increase in the number of granulocyte images. Nevertheless, since the number of lymphocytes and monocytes was less than that of granulocytes, we generated a more extensive range of reference images for these subtypes, applying fine rotation angles ranging from  $\pm 3^\circ$  up to  $\pm 19^\circ$  and  $\pm 4^\circ$  up to  $\pm 25^\circ$  for lymphocytes and monocytes, respectively [29]. The classification performance of the CNNs continuously improves when the rotation angle becomes finer, which shows the effectiveness of this rotation-based augmentation on cell images [20]. This approach resulted in increases of  $24 \times$  and  $50 \times$  in the number of lymphocyte and monocyte images, respectively. After data enhancement of the dataset, the three-type label-free WBCs dataset was established as shown in Table 1. Note that our work was label-free since in training and testing procedures we use bright-field images without any fluorescent tag.

## 2.2. Label-free WBCs classification network construction

To fully exploit the subtle differences in label-free WBC structures captured by microscopic imaging, this paper proposes a convolutional neural network with a feature fusion architecture for the classification of label-free WBCs. In contrast to conventional neural networks, this convolutional neural network fuses the low-level features extracted by the shallow layers with the high-level features extracted by the deep layers, forming fused features for label-free WBC classification. Compared to high-level features, the low-level features extracted by the shallow layers undergo fewer non-linear operations and provide a more intuitive representation of label-free WBC details. In contrast, the high-level features extracted by the deep layers contain more semantic information in the high-level semantic space, better reflecting the types of WBCs. For the classification task of label-free WBCs, the fused features formed by the integration of the two are undoubtedly a better feature representation. On one hand, they compensate for the inadequacy of low-level features in terms of semantic expression, and on the other hand, they address the issue of insufficient distinction between similar but different classes in the semantic space when only using high-level features for the original images.

As depicted in Fig. 2(f), the feature fusion neural network primarily comprises three convolutional parts. The input WBC images are convolved by thousands of kernels in these convolutional parts. The first part, comprising a convolutional layer and a maximum pooling layer, is used to extract low-level features. A larger convolutional kernel is adopted to gain as much overall information about the cell area as possible. The convolutional layer operates directly on the raw 3-channel input image, and the results are then activated by the ReLU activation function before being input to the maximum pooling layer [9]. To suppress overfitting, batch normalization (BN) is carried out after pooling. The convolutional layer comprises 96 convolutional kernels with a kernel size of  $11 \times 11$ , a stride of 4, and padding of 5. Given the larger size of the input images, we opt for larger convolutional kernels to achieve a broader receptive field, aiming to capture information across the entire cell region. With these larger kernels, using a larger stride does not lead to information loss. Moreover, it aids in reducing the number of model parameters. The second part follows a similar structure to the first one. In this section, 256 convolutional kernels are utilized for convolutional operations to extract additional intermediate features. Moreover, the sizes, strides, and padding of the convolutional kernels differ, specifically set to  $5 \times 5$ , 1, and 2, respectively. Despite the smaller size of

**Table 1**  
Fluorescent and corresponding bright-field images of WBCs.

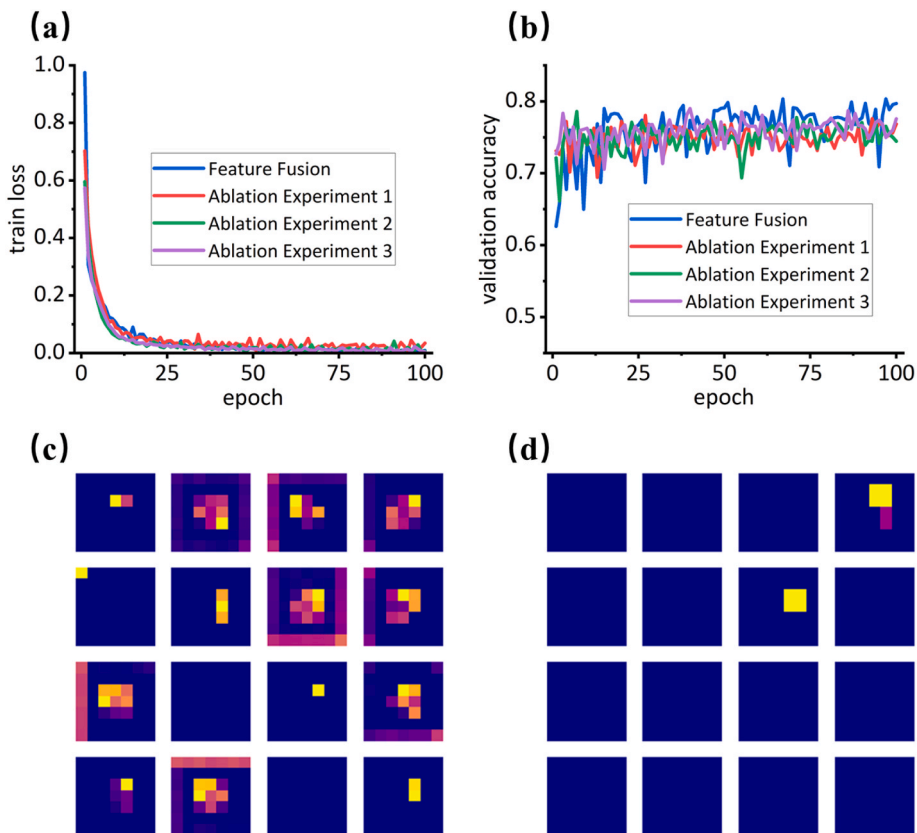
Type	Fluorescent WBC images	Bright-field WBC images	Number of images before data augmentation	Number of images after data augmentation
Granulocyte			1540	10,266
Lymphocyte			444	10,392
Monocyte			211	10,400

the convolutional kernels in this section compared to the first convolutional section, the  $5 \times 5$ -sized kernels effectively cover the entire region of a WBC, while also reducing the parameters in the model. The third part comprises three convolutional layers with 384, 384, and 256 convolutional kernels used for high-level feature extraction, as well as a maximum pooling layer. Considering that the size of the feature maps is already small, smaller convolutional kernels are utilized to reduce model parameters and prevent overfitting when the receptive field can cover a whole cell. A  $3 \times 3$  max pooling operation with a stride of 2 and padding of 1 is applied at the end of each part to reduce the size of features. This helps retain important features while reducing the risk of overfitting. We all use smaller pooling sizes and strides to prevent the loss of too much detail information of label-free WBCs. Moreover, the model has two skip paths to fuse all features of the three convolutional parts. After fusion, 608 feature maps representing the raw image from low-level to high-level, with a size of  $7 \times 7$ , are generated.  $1 \times 1$  convolution is used to fuse and downscale these feature maps to form 256 feature maps with a size of  $7 \times 7$ . Following vectorization and fully connected layers, these are used to classify different classes of WBCs.

### 3. Results and discussions

During the model training process, the Adam optimizer [29] is employed for mini-batch stochastic gradient descent optimization, with the batch size and learning rate set to 32 and  $10^{-4}$ , respectively. In addition, the coefficients for calculating the averages of gradients and their squares during training are set to 0.9 and 0.999, respectively.

To evaluate the performance of the label-free WBC classification model, this paper employs several different metrics for multi-dimensional evaluation, including recall, precision, accuracy and F1-score. Recall indicates the probability of predicting correctly that a sample is positive among actual positive samples, as shown in (1). Precision indicates the probability of the samples predicted as positive that are actually positive, as shown in (2). Higher recall and precision indicate better classification results. F1-score is the harmonic mean of recall and precision, as shown in (3). As recall and precision only evaluate samples predicted as positive, accuracy can be used as an overall evaluation metric for model prediction performance, as shown in (4). In the formulae for the above metrics, TP, TN, FP, and FN respectively represent true positives, true negatives, false positives, and false negatives. True positive (TP) indicates the number of actual positive samples predicted as positive, true negative (TN) indicates the number of actual negative samples predicted as negative, false positive (FP) indicates the number of actual negative samples predicted as positive, and false negative (FN) indicates the number of actual positive samples predicted as negative.



**Fig. 3.** (a) Training loss and (b) validation accuracy corresponding to different ablation experiments. (c) and (d) are the first 16-channel feature maps before vectorization for the control and ablation experiments, respectively.

$$Recall = \frac{TP}{TP + FN} \tag{1}$$

$$Precision = \frac{TP}{TP + FP} \tag{2}$$

$$F1score = \frac{2 \times Precision \times Recall}{Precision + Recall} \tag{3}$$

$$Accuracy = \frac{TP + TN}{TP + TN + FP + FN} \tag{4}$$

To validate the proposed label-free WBC classification network model based on feature fusion architecture, this paper initially conducted three ablation experiments, thoroughly demonstrating the effectiveness of the classification model based on feature fusion architecture in terms of classification accuracy. For the first ablation experiment, the skip path used for feature fusion following the first pooling layer was eliminated, and only the feature maps after the second and third pooling layers were fused. For the second ablation experiment, the configuration was opposite to the first one: the skip path after the first pooling layer was retained, the skip path after the second pooling layer was removed, and the feature maps after the first and third pooling layers were fused. For the third ablation experiment, the skip paths after both the first and second pooling layers were removed, leaving the entire network with a serial structure without any skip paths. The classification network with feature fusion architecture proposed in this paper was included in the experiments as a control experiment.

From Fig. 3(a) and (b), it can be observed that after 25 epochs of training, the loss values of both the ablation experiment groups and the control experiment converge to the order of  $10^{-2}$ . Comparing the validation accuracy, the ablation experiment 1 and experiment 2, which integrate some shallow features, and ablation experiment 3, which does not use feature fusion at all, all perform worse than the control experiment. The proposed feature fusion-based classification network, which serves as the control experiment, has a average validation accuracy that is 1.15 %, 0.33 %, and 1.31 % higher than that of ablation experiment 1, experiment 2, and experiment 3, respectively, indicating a better performance level. At the same time, the average validation accuracy of ablation experiment 2 is 0.82 % higher than that of ablation experiment 1. This advantage is due to the skip path post the first pooling layer providing feature maps with more original image detail information for feature fusion than the second pooling layer. After feature fusion, the classifier can better classify label-free WBCs. Comparing the loss values during the training process, the lowest training losses of the control experiment and ablation experiment 1, experiment 2, and experiment 3 are  $1.2 \times 10^{-3}$ ,  $6.6 \times 10^{-3}$ ,  $3.2 \times 10^{-3}$ , and  $3.7 \times 10^{-3}$ , respectively, which indicates that the control experiment can achieve lower training loss compared to the ablation experiment groups. Fig. 3(c) and (d) display the first 16 channels of feature maps before vectorization, using the feature fusion architecture and without using it, respectively. As seen in the visualized feature maps, the first 16 channel feature maps using feature fusion architecture contain richer information compared to those without feature fusion. The former exhibits distinctive features, while the latter only contains a small amount of high-level semantic information that is difficult for humans to comprehend at the cell locations. This difference indicates that the feature fusion model has an enhanced ability to recognize different features in cell images,

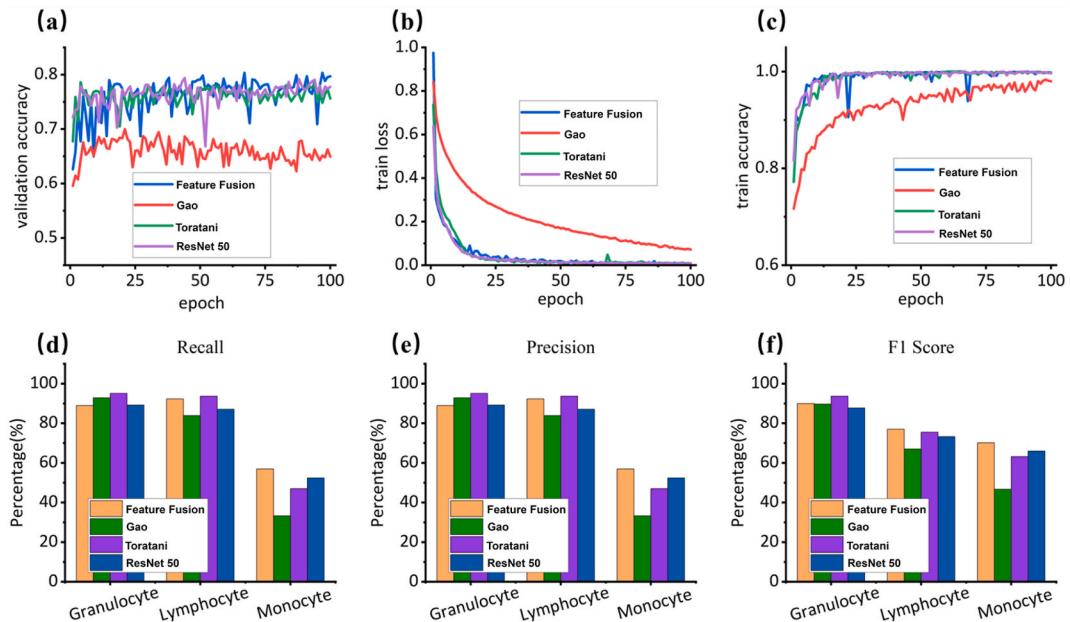


Fig. 4. (a) Validation accuracy, (b) Training loss, and (c) Training accuracy. (d) Recall (e) Precision and (f) F1 score of different models.

enabling the model to capture richer information. This information will assist the model in accurately discerning the true category of images during final classification. While the feature maps without feature fusion display nearly identical features, indicating that the model fails to capture the differences between these diverse cell images. The fused features enable the classifier to not only utilize the semantic information extracted by the high-level network when discriminating between WBC types but also take full advantage of the original image detail information extracted by the shallow network to assist in classification.

For a better comparative analysis, this paper compares the proposed label-free WBC classification model based on feature fusion with the label-free cell classification models proposed by Gao et al. [20], Toratani et al. [21], and ResNet-50 [24], which is widely used in various classification scenarios. In Fig. 4 (a), which presents a comparison of validation accuracies, it can be clearly observed that the label-free WBC classification network based on feature fusion architecture achieves higher validation accuracy compared to other deep learning cell classification works that do not use feature fusion structures. By averaging the validation accuracies during training, this paper outperforms other methods by 0.3 %, 10.5 %, and 0.3 %. This improvement in validation accuracy is attributed to the fusion of low-level features with more image detail information and high-level features with more semantic information during the training process, indicating that the proposed network with feature fusion architecture is more suitable for the classification task of label-free WBCs. At the same time, testing was conducted on the test dataset with an accuracy of 80.3 %. In Fig. 4(b), which illustrates a comparison of training loss values, the proposed model based on feature fusion architecture achieves the lowest training loss of  $2 \times 10^{-3}$ , despite all models eventually reaching low training losses. Fig. 4(d)–(f) display comparisons of recall, precision, and F1 scores for the four experimental models, and it is evident that in terms of F1 scores for the three different categories of label-free WBCs, the network based on feature fusion proposed in this paper significantly outperforms other related works and obtains the highest F1 score. This excellent performance is not only due to the uniquely designed network structure but also the powerful feature representation constructed by the feature fusion architecture.

#### 4. Conclusions

To address the problem of insufficient utilization of the detailed features of WBC images by the existing deep neural network, this work introduces a label-free WBCs classification network with feature fusion structure to classify them. The performance of our proposed model achieves an optimal accuracy of 80.3 %, surpassing other models that lack feature fusion capabilities. At the same time, our approach eliminates the need for costly and large sample volume, as required by flow cytometers, and avoids the necessity of fluorescent staining for cell labeling, which was previously employed in image analysis-based WBC classification using fluorescent images. By simplifying the cell detection process and eliminating complex procedures such as fluorescent staining, our proposed method offers a practical solution for precise and efficient WBC classification. Consequently, the development of an automatic, label-free, and damage-free WBC classification network for more precise and effective analysis holds significant potential to promote the popularization of a miniaturized flow cytometer for POC diagnostic applications.

At last, the limitations of this work and future directions of label-free WBC research are discussed. Firstly, how to conveniently and precisely obtain the true labels of unlabeled WBCs, completely eliminating the staining step is a key issue. Secondly, considering the introduction of more image augmentation methods to enhance the model's robustness and improve its generalization ability across different datasets is also worth exploring. Additionally, the use of three-dimensional WBC images which containing more information for classification could be considered. Finally, it is important to note that WBCs may exhibit different morphologies under different immune states, and future research needs to address this issue to ensure their accuracy and reliability in medical applications.

#### CRedit authorship contribution statement

**Jin Chen:** Conceptualization, Data curation, Formal analysis, Investigation, Methodology, Writing – original draft, Writing – review & editing. **Liangzun Fu:** Data curation, Formal analysis, Investigation, Validation, Visualization, Writing – review & editing. **Maoyu Wei:** Conceptualization, Data curation, Investigation, Visualization, Writing – original draft. **Sikai Zheng:** Data curation, Investigation, Validation. **Jingwen Zheng:** Investigation, Validation. **Zefei Lyu:** Investigation, Validation. **Xiwei Huang:** Conceptualization, Funding acquisition, Methodology, Project administration, Resources, Software, Supervision, Validation, Writing – review & editing. **Lingling Sun:** Resources, Writing – review & editing.

#### Declaration of competing interest

The authors declare that they have no known competing financial interests or personal relationships that could have appeared to influence the work reported in this paper.

#### Acknowledgments

This work was supported by the National Natural Science Foundation of China (Grant No. 62271184, 61827806), Zhejiang Provincial Natural Science Foundation of China (Grant No. LZ22F010007), National Key R&D Program of China (2022YFD2000100).

## References

- [1] V. Peltola, J. Mertsola, O. Ruuskanen, Comparison of total white blood cell count and serum C-reactive protein levels in confirmed bacterial and viral infections, *J. Pediatr.* 149 (2006) 721–724.
- [2] B. George-Gay, K. Parker, Understanding the complete blood count with differential, *J. PeriAnesthesia Nurs.* 18 (2003) 96–117.
- [3] C. Petchakup, H.M. Tay, K.H.H. Li, H.W. Hou, Integrated inertial-impedance cytometry for rapid label-free leukocyte isolation and profiling of neutrophil extracellular traps (NETs), *Lab Chip* 19 (2019) 1736–1746.
- [4] R. Hoffman, E.J. Benz Jr., L.E. Silberstein, H. Heslop, J. Anastasi, J. Weitz, *Hematology: basic principles and practice*, 6th ed, Elsevier Health Sciences, 2013, pp. 639–655.
- [5] H. Jeon, M. Wei, X. Huang, J. Yao, W. Han, R. Wang, X. Xu, J. Chen, L. Sun, J. Han, Rapid and label-free classification of blood leukocytes for immune state monitoring, *Anal. Chem.* 94 (2022) 6394–6402.
- [6] B. Jundi, H. Ryu, D.-H. Lee, R.-E.E. Abdunour, B.D. Engstrom, M.G. Duvall, A. Higuera, M. Pinilla-Vera, M.E. Benson, J. Lee, Leukocyte function assessed via serial microlitre sampling of peripheral blood from sepsis patients correlates with disease severity, *Nat. Biomed. Eng.* 3 (2019) 961–973.
- [7] W. Zhang, Y. Li, B. Chen, Y. Zhang, Z. Du, F. Xiang, Y. Hu, X. Meng, C. Shang, S. Liang, X. Yang, W. Guan, Fully integrated point-of-care blood cell count using multi-frame morphology analysis, *Biosens. Bioelectron.* 223 (2022) 115012.
- [8] A. Adan, G. Alizada, Y. Kiraz, Y. Baran, A. Nalbant, Flow cytometry: basic principles and applications, *Crit. Rev. Biotechnol.* 37 (2017) 163–176.
- [9] J. Chen, X. Huang, X. Xu, R. Wang, M. Wei, W. Han, J. Cao, W. Xuan, Y. Ge, J. Wang, Microfluidic particle separation and detection system based on standing surface acoustic wave and lensless imaging, *IEEE (Inst. Electr. Electron. Eng.) Trans. Biomed. Eng.* 69 (2021) 2165–2175.
- [10] R. Wang, X. Huang, X. Xu, J. Sun, S. Zheng, X. Ke, J. Yao, W. Han, M. Wei, J. Chen, A standalone and portable microfluidic imaging detection system with embedded computing for point-of-care diagnostics, *IEEE Sensor. J.* 22 (2022) 6116–6123.
- [11] X. Huang, D. Xu, J. Chen, J. Liu, Y. Li, J. Song, X. Ma, J. Guo, Smartphone-based analytical biosensors, *Analyst* 143 (2018) 5339–5351.
- [12] M. Nassar, M. Doan, A. Filby, O. Wolkenhauer, D.K. Fogg, J. Piasecka, C.A. Thornton, A.E. Carpenter, H.D. Summers, P. Rees, H. Hennig, Label-free identification of white blood cells using machine learning, *Cytometry A* 95 (2019) 836–842.
- [13] S. Nazlibilek, D. Karacar, T. Ercan, M.H. Sazli, O. Kalender, Y. Ege, Automatic segmentation, counting, size determination and classification of white blood cells, *Measurement* 55 (2014) 58–65.
- [14] N. Dong, Q. Feng, M. Zhai, J. Chang, X. Mai, A novel feature fusion based deep learning framework for white blood cell classification, *J. Ambient Intell. Hum. Comput.* (2023) 1–13.
- [15] A. Girdhar, H. Kapur, V. Kumar, Classification of white blood cell using convolution neural network, *Biomed. Signal Process Control* 71 (2022) 103156.
- [16] C. Jung, M. Abuhamad, J. Alikhanov, A. Mohaisen, K. Han, D. Nyang, W-Net: a CNN-Based Architecture for White Blood Cells Image Classification, 2019 arXiv preprint arXiv:1910.01091.
- [17] S.H. Rezatofghi, H. Soltanian-Zadeh, Automatic recognition of five types of white blood cells in peripheral blood, *Comput. Med. Imag. Graph.* 35 (2011) 333–343.
- [18] C.B. Wijesinghe, D.N. Wickramarachchi, I.N. Kalupahana, R. Lokesh, I.D. Silva, N.D. Nanayakkara, Fully automated detection and classification of white blood cells, in: 2020 42nd Annual International Conference of the IEEE Engineering in Medicine & Biology Society (EMBC), IEEE, 2020, pp. 1816–1819.
- [19] K. Simonyan, A. Zisserman, Very Deep Convolutional Networks for Large-Scale Image Recognition, 2014 arXiv preprint arXiv:1409.1556.
- [20] Z. Gao, L. Wang, L. Zhou, J. Zhang, HEp-2 cell image classification with deep convolutional neural networks, *IEEE journal of biomedical and health informatics* 21 (2016) 416–428.
- [21] M. Toratani, M. Konno, A. Asai, J. Koseki, K. Kawamoto, K. Tamari, Z. Li, D. Sakai, T. Kudo, T. Satoh, A convolutional neural network uses microscopic images to differentiate between mouse and human cell lines and their radioresistant clones, *Cancer Res.* 78 (2018) 6703–6707.
- [22] Y. Li, B. Cornelis, A. Dusa, G. Vanmeerbeeck, D. Vercrucy, E. Sohn, K. Blaszkiwicz, D. Prodanov, P. Schelkens, L. Lagae, Accurate label-free 3-part leukocyte recognition with single cell lens-free imaging flow cytometry, *Comput. Biol. Med.* 96 (2018) 147–156.
- [23] Y. Young, Label-free white blood cell classification using refractive index tomography and deep learning, *BME frontiers* 2021 (2021) 9893804.
- [24] K. He, X. Zhang, S. Ren, J. Sun, Deep residual learning for image recognition, in: *Proceedings of the IEEE Conference on Computer Vision and Pattern Recognition*, 2016, pp. 770–778.
- [25] A. Rigon, P. Soda, D. Zennaro, G. Iannello, A. Afeltra, Indirect immunofluorescence in autoimmune diseases: assessment of digital images for diagnostic purpose, *Cytometry Part B: Clinical Cytometry: The Journal of the International Society for Analytical Cytology* 72 (2007) 472–477.
- [26] M. Lippeveld, C. Knill, E. Ladlow, A. Fuller, L.J. Michaelis, Y. Saeys, A. Filby, D. Peralta, Classification of human white blood cells using machine learning for stain-free imaging flow cytometry, *Cytometry A* 97 (2020) 308–319.
- [27] H. Jeon, B. Jundi, K. Choi, H. Ryu, B.D. Levy, G. Lim, J. Han, Fully-automated and field-deployable blood leukocyte separation platform using multi-dimensional double spiral (MDDS) inertial microfluidics, *Lab Chip* 20 (2020) 3612–3624.
- [28] N. Otsu, A threshold selection method from gray-level histograms, *IEEE transactions on systems, man, and cybernetics* 9 (1979) 62–66.
- [29] M.M. Krell, S.K. Kim, Rotational data augmentation for electroencephalographic data, in: 2017 39th Annual International Conference of the IEEE Engineering in Medicine and Biology Society (EMBC), IEEE, 2017, pp. 471–474.